Int J Adv Manuf Technol (2015) 79:1425–1441
DOI 10.1007/s00170-015-6932-6

ORIGINAL ARTICLE

On experimental optimization of friction stir welding of aluminum 6061: understanding processing-microstructure-property relations

M. Nourani · A. S. Milani · S. Yannacopoulos

Received: 3 November 2014 / Accepted: 20 February 2015 / Published online: 4 March 2015

Abstract A comprehensive investigation into processing-microstructure-property relations for optimization of ultimate tensile strength (UTS) of friction stir welded aluminum 6061 plates is presented. A customized experimental setup has been employed to measure temperature at multiple points of welded plates as well as the friction stir welding (FSW) tool axial force, transverse force, torque, and temperature under various combinations of process parameters. After performing a set of FSW tests based on a full factorial design, X-ray and ultrasonic tests were employed to detect process-induced failure in test samples. Using design of experiments, the main effects and percentage contributions of the process parameters on the maximum UTS were then identified. During the latter analysis, a new methodology is proposed to cope with the effect of "variable" axial force, as it is often uncontrollable during FSW tests. Samples with the highest and lowest UTS were selected and examined in more detail by comparing their fracture surfaces using scanning electron microscopy (SEM), as well as their grain size distributions using electron back scattered diffraction (EBSD) and microhardness experiments. Finally, through the observed microstructure, temperature distribution, and welding force, it could be explained why the UTS and microhardness are found to notably vary between sample sof different RPM and weld speeds.

Keywords Friction stir welding · Processing-microstructure-property relations · Design of experiments · Optimization

M. Nourani · A. S. Milani (✉) · S. Yannacopoulos
School of Engineering, University of British Columbia, Kelowna, Canada
e-mail: abbas.milani@ubc.ca

1 Introduction

Since its invention at the Welding Institute of UK in December 1991, there have been widespread applications of friction stir welding (FSW) in a range of industries producing, e.g., airplanes fuselage, ship deck, automobiles BIW, and trains in chassis. In FSW, a rotating tool consisting of a pin and a shoulder is pressed against the matched ends of two plates/parts to be welded, while traversing along the weld centerline. A specific advantage of this particular joining procedure is that the heat transfer is accomplished by the heat of deformation of material close to the tool and there is no need to melt the material, i.e., the weld is made in a solid state. Over the past two decades, there have been numerous experimental studies on different FSW processes of similar and dissimilar alloys.

Regarding the FSW of similar alloys, Yan et al. [1] studied the effects of weld tool rotational speed, welding speed, and *z*-axis force on the nugget microstructure, nugget tensile properties, and heat-affected zone hardness during friction stir welding of aluminum 2524-T351. Mahoney et al. [2] evaluated the feasibility of friction stir welding of SiC particulate reinforced 6092 aluminum composites, by observing the microstructure of the weld nugget, distribution of particulates, tensile mechanical properties, failure sites and type of fracture surfaces, and the weld hardness profile. Commin et al. [3] studied the temperature evolution during FSW of AZ31 Mg alloy and the resulting residual stress to gain a better understanding of the mechanisms involved in this manufacturing process. The relationship between the processing parameters, the heat and plastic deformation produced, and the resulting microstructure and mechanical properties was investigated. Lee et al. [4] studied the feasibility of FSW for joining of copper. They also investigated the grain size, microhardness, and tensile properties of the samples. Konkol et al. [5] studied

feasibility of FSW of HSLA-65 by performing transverse tensile and bending tests, hardness, Charpy V-notch toughness, salt spray corrosion testing, and metallographic evaluations. Posada et al. [6] studied the FSW of stainless steel 304 with different process parameters. They evaluated microstructure (optical and scanning electron microscopy (SEM)) and hardness as a function of welding energy. Nandan et al. [7] investigated heat transfer and viscoplastic flow during FSW of Ti-6AI-4V alloy and validated their model by temperature and torque measurements.

Regarding dissimilar alloys, Aval et al. [8] evaluated thermomechanical behavior and microstructural events in friction stir welding of AA6061-T6 to AA5086-O aluminum alloys. Thermomechanical responses of materials during the process were predicted employing a three-dimensional model; then, mechanical properties and microstructures of the weld zone were studied with the aid of experimental observations and model predictions. Taban et al. [9] used tensile tests, metallography, microhardness testing, SEM, energy dispersive spectroscopy (EDS), X-ray elemental mapping, focused ion beam (FIB) with ultra high resolution SEM, and transmission electron microscopy (TEM) to study the friction stir welding of 6061-T6 aluminum to AISI 1018 steel. Da Silva et al. [10] studied the effect of joining parameters on the mechanical and microstructural characteristics of dissimilar overlap FSW of 2.5-mm-thick AA 1050 aluminum alloy to 1.8-mm-thick 22MnB5 Al–Si-coated boron steel. McLean et al. [11] studied the microstructure in FSW of magnesium alloy AZ31B to aluminum 5083 alloy. Somasekharan et al. [12] studied the microstructure of FSW of different AZ91D to AM60B magnesium alloys. Uzun et al. [13] investigated microstructure, hardness, and fatigue properties of friction stir welded 6013 aluminum alloy and X5CrNi18-10 stainless steel. Ouyang et al. [14] studied temperature distribution and microstructural evolution in the friction stir welding of 6061-T6 aluminum alloy to copper. Dressler et al. [15] studied microstructure, hardness, and tensile strength of the butt joint FSW of titanium alloy TiAl6V4 and aluminum alloy 2024-T3. Chung et al. [16] investigated friction stir welded butt joints of reduced-activation ferritic/martensitic steel (RAF/M) F82H and austenite stainless steels. They considered the effect of the tool and plate positions to prohibit the mixing of the F82H and austenite stainless steels and studied the microstructure, microhardness, and mechanical properties of the welded samples.

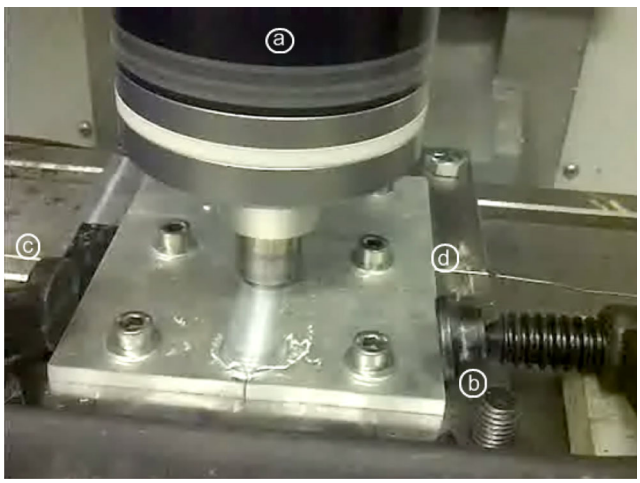

Fig. 1 FSW device (**a**) and test fixture (**b**) with two embedded thermocouples (**c**) and (**d**)

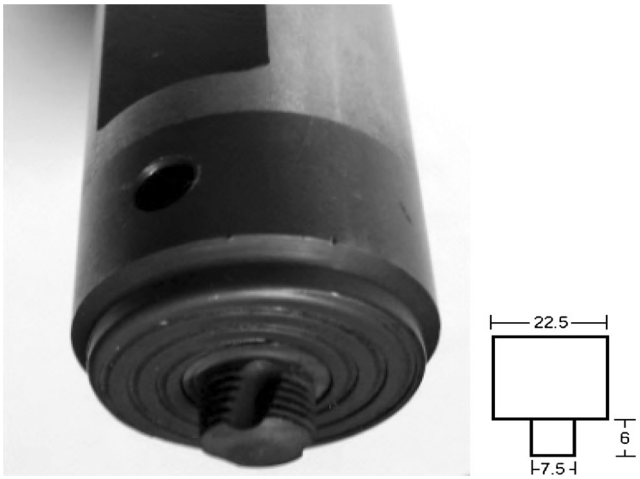

Fig. 2 Selected FSW tool pin and shoulder (dimensions in mm) made from tool steel

Through the past works above, the majority of experimental studies on FSW have considered the weld hardness, mechanical properties (such as ultimate tensile strength), and microstructure, and fatigue properties. There have also been a few other investigations considering residual stresses [17], weld texture [18], and corrosion behavior [19] of the FSW samples. Limited works have been reported, however, on using a systematic design of experiment (DOE) along with statistical analysis to identify the underlying processing-microstructure-property relationship during optimization of specific process outputs. This can be also very important in evaluating and improving numerical/surrogate models used for prediction of expensive FSW processes [20–22].

Table 1 Friction stir welding process parameters used for different samples; based on this table in subsequent sections, sample numbers will be referred as 1n, 2n,…, 9n and B2

Weld speed	Tool rotational speed		
	1000 RPM	1400 RPM	1800 RPM
45 (mm/min)	1n	2n	3n
60 (mm/min)	4n	5n	6n
75 (mm/min)	7n	8n	9n
As received (i.e., parent material)	B2		

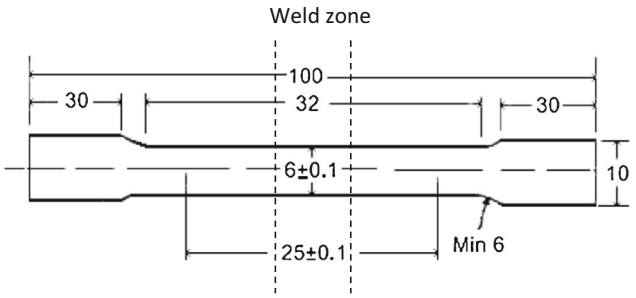

Fig. 3 Tensile test sample perpendicular to the weld line in middle (dimensions in mm)

The objective of the present article is to perform an investigation into processing-microstructure-property relationship of aluminum 6061 through a set of designed FSW and material characterization experiments, while evaluating capabilities of a recent multiphysics model [22] in predicting experimental observations. The specific process output variable was chosen to be the ultimate tensile strength. During the DOE analysis and optimization, in order to be able to perform a standard ANOVA analysis, a new approach will be proposed via multiple regression to cope with the effect of uncontrolled axial force during the FSW tests.

2 Methodology

2.1 FSW test equipment

A LowStir™ device was employed for FSW tests with a CNC milling machine as shown in Fig. 1. The FWS unit had the following specifications:

- Axial force (F_z) up to 50 kN
- Transverse force or weld force (F_{xy}) up to 25 kN
- Torque (M_z) up to 100 Nm
- Rotational speedup to 3,000 RPM

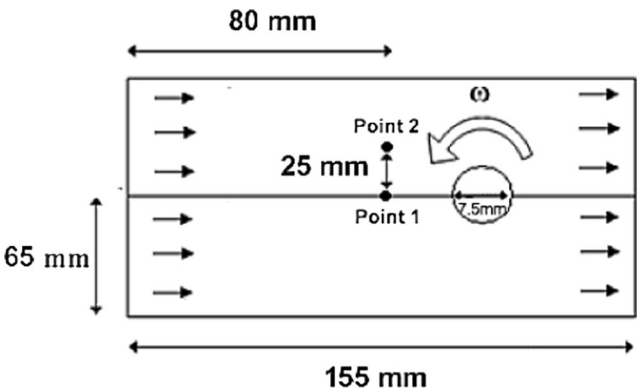

Fig. 4 Points where temperature was measured in the back of the aluminum plates during FSW tests

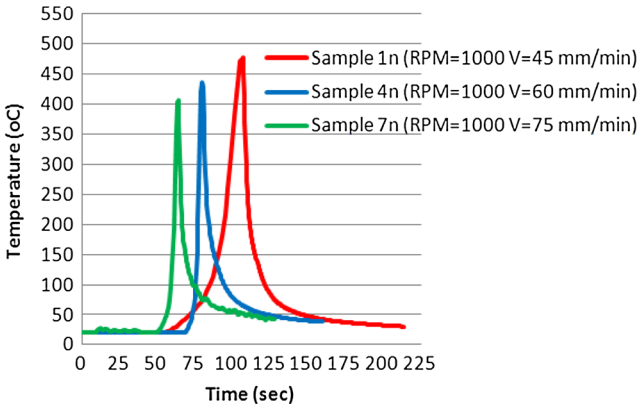

Fig. 5 Temperature measurements of samples at the middle of the weld line on back of the plates at different weld speeds and a constant RPM= 1,000

- Weld speed is limited by the feed rate of our CNC milling machine which is from 0.5 to 20 mm/s

Among different tool types (MX-Triflat™ and MX-Triflute™), the selected FSW tool was the Mx-Triflute™ pin and the single spiral scrolled shoulder with the dimensions shown in Fig. 2. For welding, 155×65×6.5 mm^3 aluminum 6061-T6 plates were used with the weld line parallel to the rolling direction (Fig. 1).

2.2 Design of experiments

Different process parameters (RPM and weld speed) were chosen for different FSW samples according to Table 1. Efforts were made to keep the axial force constant in different samples during FSW tests by choosing a fixed penetration of 0.1 mm of the shoulder into the plates. However, it was hard to maintain a fully constant axial force between different welding tests with the open-loop axial force control test setup. Hence, the variation of normal force had to be dealt with in the subsequent statistical analysis (Section 3.3.1).

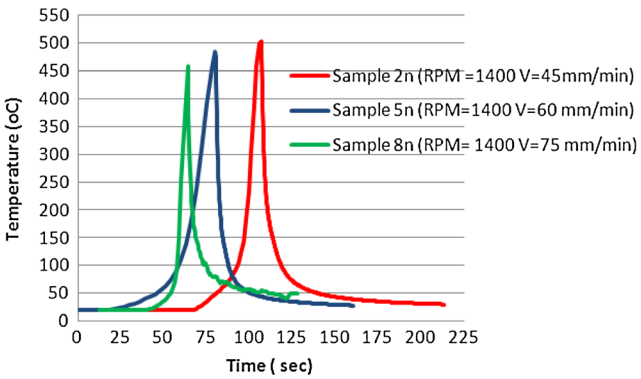

Fig. 6 Temperature measurements of samples at the middle of the weld line on back of the plates at different weld speeds and a constant RPM= 1,400

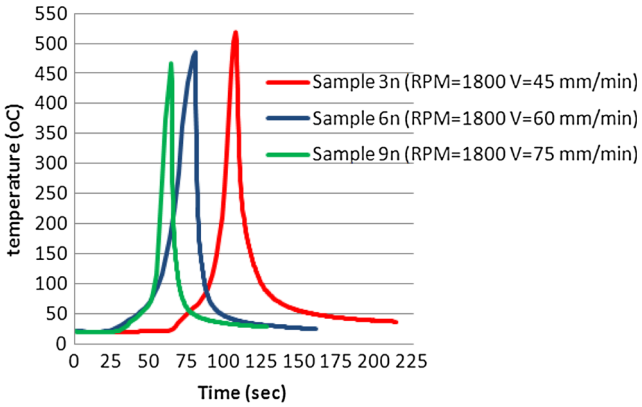

Fig. 7 Temperature measurements of samples at the middle of the weld line on back of the plates at different weld speeds and a constant RPM= 1,800

In all the tests, the tool plunge rate was 15 mm/min, tool dwell time was 10 s, the weld length was 125 mm that started and ended 15 mm from edges of the plates, and the tool exert rate was 15 mm/min. For tensile testing, a water jet machine was used to cut the samples perpendicular to the weld line according to subsize specimen dimension of ASTM E8-M standard as shown in Fig. 3. For each friction stir welding condition (i.e., under a specific combination of process parameters), two tensile samples were machined and tested.

2.3 Temperature and force measurements

During FSW experiments, the temperatures of two points at the back of the plates were recorded as shown in Fig. 4 using K-type thermocouples and a Fourier DBSA720 data acquisition system. The tool axial force, transverse force, torque, and temperature were recorded during the tests using the wireless data transferring capability of the LowStir™ device.

2.4 X-ray and ultrasonic of FSW welds

All welded plates were examined using X-ray or ultrasonic inspection by a certified inspector at Kelowna Flightcraft Ltd., BC, Canada. Subsequently, the tensile specimens were cut from welded regions with no significant failure indication. For ultrasonic inspection, ASTM E164-08 standard was used.

2.5 Tensile tests

An Instron3385H tensile test machine was used with a maximum load capacity of 250 kN at across head speed of 2.5 mm/min. After tensile tests in all welded samples, the samples with the highest and lowest ultimate tensile strength (UTS) values were chosen for further examinations.

2.6 Scanning electron microscopy (SEM) of fracture surfaces

A Tescan Mira3 XMU Field Emission Scanning Electron Microscope was employed in order to study the morphology of fracture surfaces of selected tensile samples with the highest and lowest UTS values.

2.7 Microstructure analysis with electron back scattered diffraction (EBSD)

An Oxford AZtecHKL EBSD system was used in order to study the grain size distribution on mid plane of the advancing side of the samples with the highest and the lowest UTS values. Earlier studies [22] show that the maximum flow rate during FSW is normally located near the top of the advancing side of the pin. For preparation of each EBSD test, a weld cross section was cut from the weld line and was mounted at the advancing side of weld. Subsequently, Struers™ polishing and electropolishing machines were used to polish the sample. For the latter, first a 320 μm emery paper was used for 60 s and then a polishing mat with 100 μm Al_2O_3 suspension for 20 s and 10 μm diamond paste with emery paper for 30 s. In electropolishing, A_2 solution in the manual mode was employed with a voltage of 12 V for 15 s. The A_2 solution composition was as follows:

- Distilled water (90 ml)
- Ethanol (ethyl alcohol) (730 ml)
- Ethylene glycol monobutyl ether (l00 ml)
- Perchloric acid (78 ml)

The perchloric acid had to be added to the mixture of ethanol, ethylene glycol monobutyl ether, and water immediately before use.

Table 2 Summary of FSW maximum temperature at the middle of the weld line on back of different tested samples

Maximum temperature (°C)	1000 RPM	1400 RPM	1800 RPM
45 (mm/min)	476	502	519
60 (mm/min)	438	484	485
75 (mm/min)	407	441	467

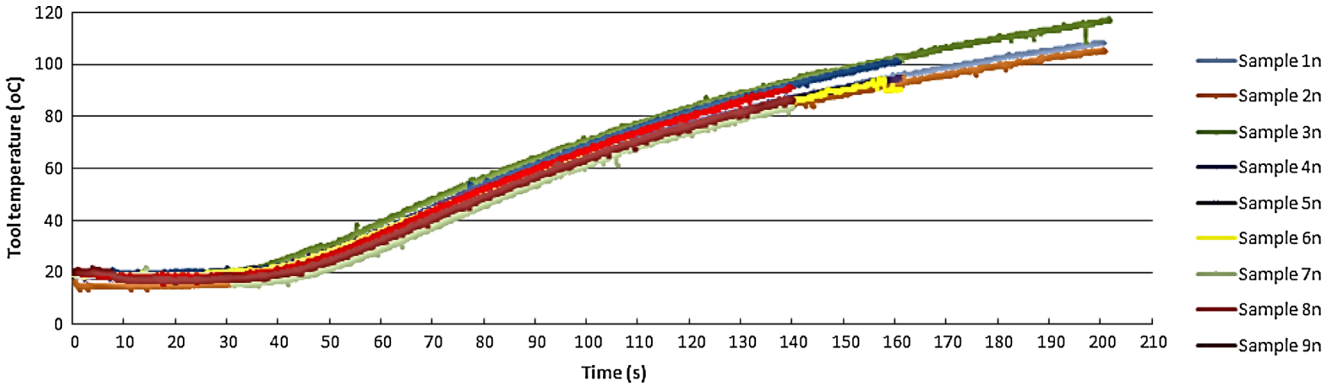

Fig. 8 Tool temperature during FSW tests on different samples

The scanned region at each time frame had a 1,350× 400 μm^2 area. In each subsequent frame, the beam was moved 1,250 μm toward the next point in order to have a 100 μm overlap between the images, which later merged/stitched to form a continuous image of the grain size distribution on the mid plates of samples with the highest and the lowest UTS values. The number of grains at each EBSD frame was also counted on three points (two sides and the middle point) within a 77 μm horizontal line.

2.8 Microhardness study

A Qualitest QV-1000 microhardness test equipment was used with 500 g force and 15 s dwell time in order to measure the Vickers microhardness in 0.5-mm intervals on the mid plane of the advancing side of the weld cross section of samples with the highest and the lowest UTS.

3 Results and discussion

3.1 Temperature and force measurements

In this section, we present the temperature test data at the middle of the back of plates on the weld line of all tested samples at point 1 (Fig. 4), along with the corresponding tool axial force, transverse force, and torque measurements under various processing conditions per Table 1.

Figures 5, 6 and 7 illustrate comparisons of temperature measurements at point 1 under different weld speeds of 45, 60, and 75 mm/min and the tool RPMs of 1,000, 1,400, and 1, 800. As seen in these figures, the maximum temperature at point 1 in the plates is reduced by increasing the weld (transverse) speed given a tool RPM. The maximum variable temperature at point 1 in different samples is also included in Table 2, which shows that this FSW output variable is increased by increasing the tool RPM given a weld speed. The highest maximum temperature of 519 °C has occurred in sample 3n (hot weld) and the lowest maximum temperature of 407 °C is in sample 7n (cold weld), which are highlighted in red and green colors in Table 2, respectively. Note that the resulting maximum temperature difference between these two extreme processing conditions is as high as 112 °C, which can have close effect on resulting microstructure and mechanical properties of the weld as will be discussed through Sections 3.3 to 3.6.

In Fig. 8, the tool temperature in different samples has been measured at far end of the tool shaft from the weld zone (somewhere near point a in Fig. 1). Temperature results

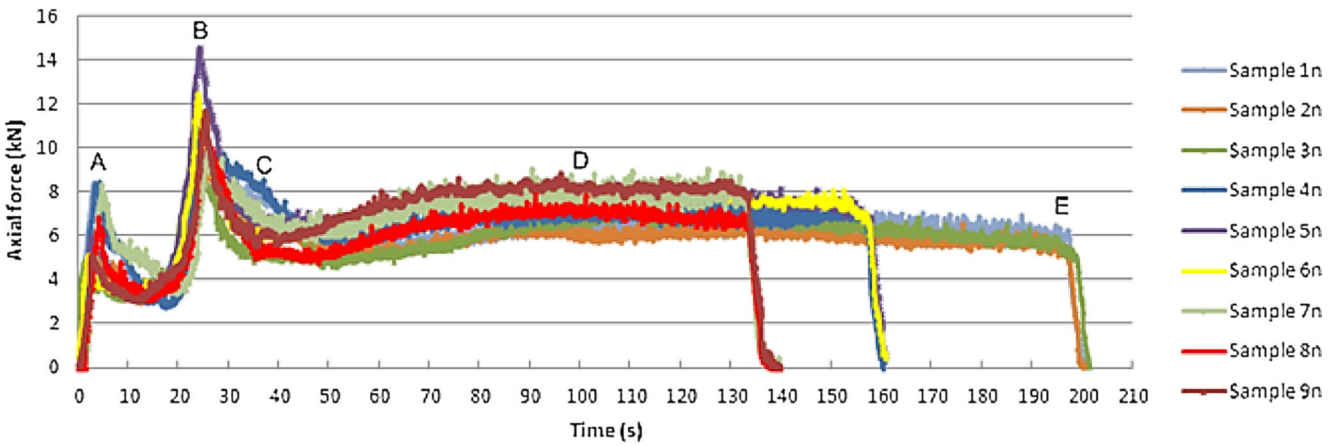

Fig. 9 Tool axial force on different samples during FSW tests with critical points of response curves marked as A, B, C, D, and E

Table 3 Average axial force of the tool in the steady-state response phase of the FSW samples

Average axial force (kN)	1000 RPM	1400 RPM	1800 RPM	Row Averages
45 (mm/min)	6.33	6.08	6.19	6.19
60 (mm/min)	7.10	7.70	7.14	7.14
75 (mm/min)	7.14	6.64	7.52	7.52
Column Averages:	7.12	6.80	6.95	Total Average: 6.95

reconfirm that samples 3n and 7n (see also Table 1) correspond to the hot weld and cold weld states, respectively.

Figure 9 shows the measured tool axial force of different samples. It can be noticed that the highest axial force during the steady-state phase of the curves (point D) belongs to sample 7n (cold weld) and the lowest axial force has occurred in sample 3n (hot weld). There are five critical points in the axial force curve during FSW as noted as A, B, C, D, and E in Fig. 9. Point (A) shows the maximum axial force when the tool pin starts the plunge inside the plates. Point (B) is the point when the tool shoulder reaches the fixed penetration of 0.1 mm inside the plates during the plunge phase. Point (C) is the end of dwell phase when the plates are hot enough to start the FSW after 10 s of dwell time. Point (D) is when the FSW reaches the steady-state condition, and point (E) is when the tool starts exiting the plates. A–B is called the plunge phase, B–C is the dwell phase, C–D is the welding phase, and D–E is the exist phase. As seen in Fig. 9, it is hard to keep a constant axial force in test samples using an open-loop force control system of FSW setup (despite a fixed penetration of 0.1 mm). The source of this noise in the axial forces can be one or combination of the following factors:

1. The tool wearing during the process which changes the reference point during tool setup,
2. Operator's error,
3. Plates thickness tolerances,
4. Vibration effects, and
5. Formation of different excess material from weld zone (flush) during FSW.

In more advanced setups, one could possibly use a closed-loop control system which changes the tool penetration inside the plates in order to keep a constant axial force during FSW tests, though this is often impractical or too expensive. The average axial forces in the steady-state phase of the response curves are reported in Table 3. The highest average axial force is generated in sample 5n, and the lowest value is seen in sample 2n, which are highlighted in Table 3 in green and red colors, respectively.

Figure 10 shows the tool torque measurements in different samples with the same critical points of A, B, C, D. and E as in Fig. 9. The highest torque is seen in sample 7n (cold weld) and also sometimes in sample 4n (second cold weld). The lowest torque belongs to sample 3n (hot weld). Also, when the RPM is increased under a constant weld speed, the torque is decreased which is because of the increase in heat input during FSW.

Figure 11 shows the measured transverse force of different samples during FSW tests. The minimum transverse force is seen in sample 4n, and the maximum transverse force belongs to samples 6n and 9n with the highest RPM and sometimes to samples 7n (cold weld) and 1n. The highest transverse force in samples 6n and 9n or 7n can be a result of higher excess

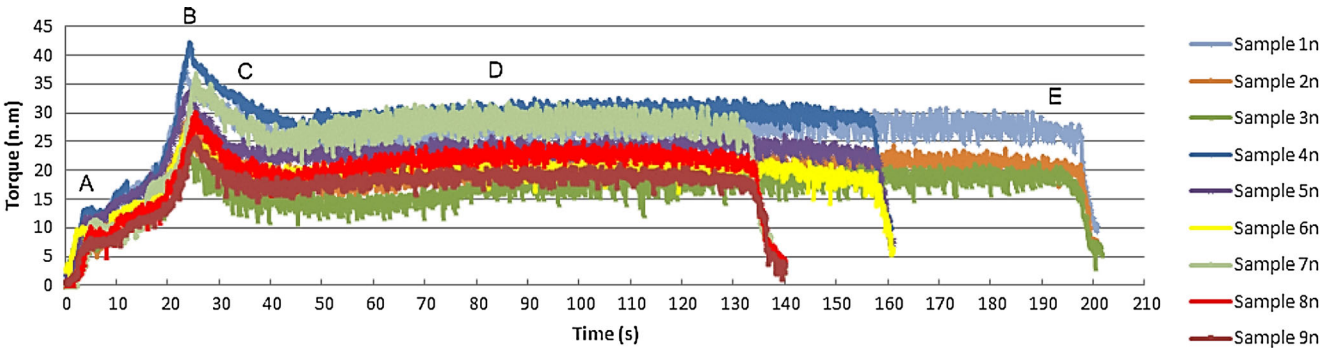

Fig. 10 Tool torque at different samples during FSW tests with critical points of A, B, C, D, and E

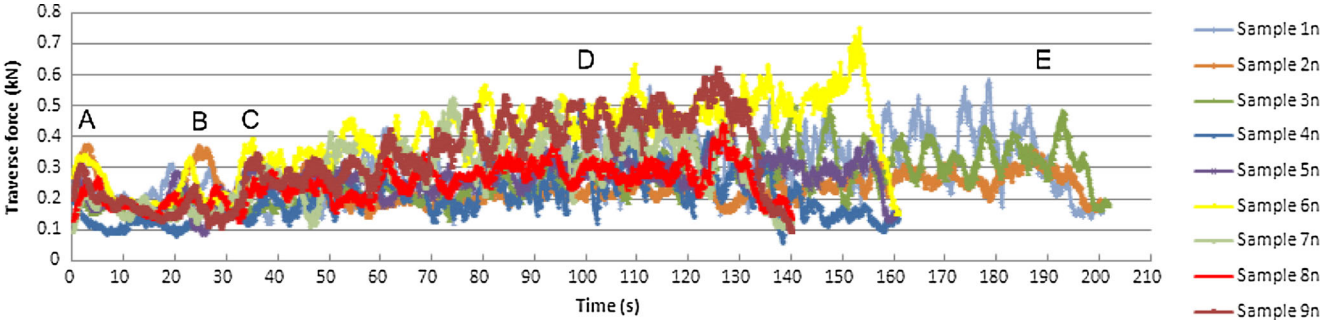

Fig. 11 Tool transverse force at different samples during FSW tests with critical points of A, B, C, D, and E

material from the weld (flush) or higher material flow stress during the process. The distance between two consecutive transverse force peaks in Fig. 11 is equal to the time of one advance per rotation.

3.2 X-ray and ultrasonic

After completing the FSW experiments, X-ray and ultrasonic tests were performed on the welded samples to investigate if there is any evidence of failure on the weld regions. Figure 12 shows the samples after the FSW experiments. Samples 1n, 6n, and 9n had a few areas along the weld line with lack of diffusion, among which sample 9n had the highest lack of diffusion volume. If we examine Fig. 12 more closely, it is clear that samples 3n, 6n, and 9n with the highest tool RPM values and sample 5n with the highest average axial force have had a high volume of excess material (flush) from the weld zone (shown with star signs in Fig. 12). It is interesting that in samples 1n, 6n, and 9n which had showed some failure in X-ray and ultrasonic tests, we observed a relatively higher transverse force during FSW (Fig. 11), which can be a direct indication of higher excess material from the weld zone.

3.3 Tensile tests

After cutting two tensile samples from each FSW plate (Fig. 13) as well as the as-received (parent) plate, tensile tests were performed and compared for their UTS values. The as-received 6061-T6 plate showed a UTS of 348.2 MPa. The highest UTS in the FSW samples had a UTS equal to 76 % of the as-received plate. The lower UTS of welded samples compared to the parent metal is a result of overaging in *heat treatable* aluminum alloys such as Al 6061 (due to the heat during welding and its effect on precipitates size, coherency to matrix and distribution). The values of UTS of different samples are summarized in Table 4. The minimum UTS belongs to sample 3n (hot

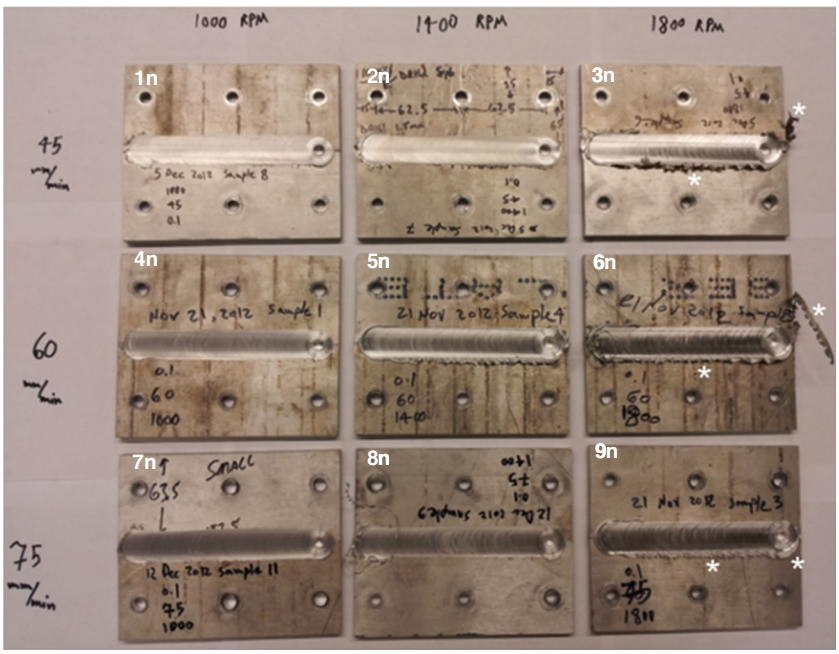

Fig. 12 FSW samples with different process parameters of weld speed and tool RPM (the excess material is shown with *white stars*)

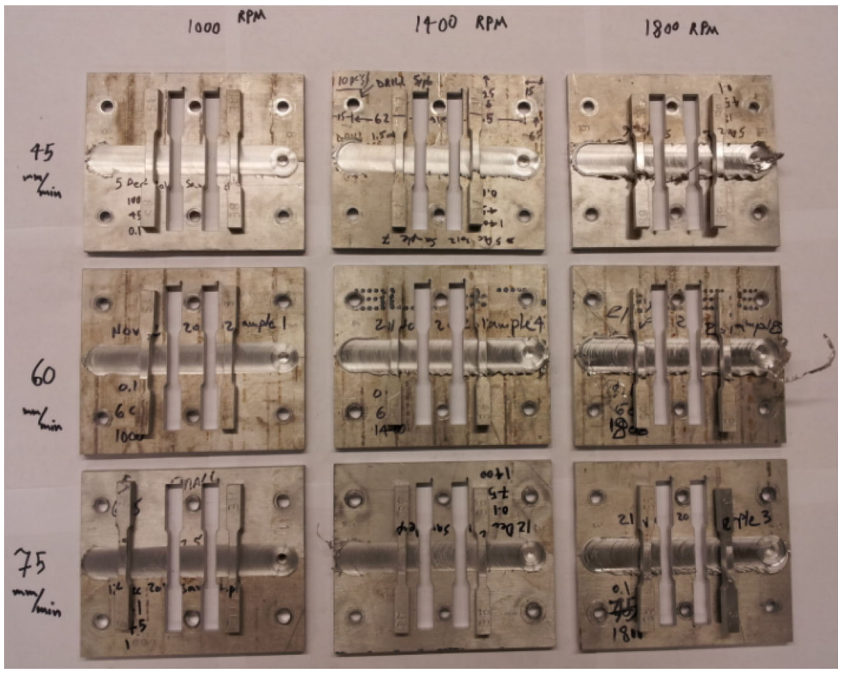

Fig. 13 Tensile samples cut from FSW samples with different controlled process parameters (weld speed and tool RPM)

weld), and the maximum UTS is seen in both samples 5n (with the highest average axial force per Table 3) and 4n (the second cold weld per Table 2) with a small difference in the UTS of the latter two samples. Following the hypothesis in study [20], one would expect to see the lowest UTS in the hot weld (sample 3n) which is in agreement with the results here in Table 4. On the other hand, the highest UTS should theoretically occur in the cold weld (sample 7n), but this is not the case here; however, sample 4n which was the second cold weld sample is among those with the highest UTS. With further investigation of fracture surfaces, this discrepancy was sought to be the result of the low mechanical bounding in the very cold weld of 7n (to be discussed in more detail in Section 3.4; Fig. 17).

3.3.1 Factor effect analysis

In order to use a standard ANOVA analysis and statistically estimate the effects of controlled process parameters (namely RPM and weld speed) on the UTS of the FSW samples, first it was necessary to eliminate the effect of uncontrolled axial force factor during the tests (note that the row averages and column averages are different in Table 3, and hence, a standard DOE factor analysis cannot be performed). To address this problem, a multiple regression model using data points of Tables 1, 3, and 4 were established, where several second-order polynomials with up to eight different constants (given that here we have nine data points/FSW configurations) were tried and compared for their coefficient of determinations. In doing so,

Table 4 Ultimate tensile strength of different FSW samples (minimum, maximum, and average); *red* and *green highlights* represent the extreme conditions under the maximum UTS criterion

UTS (MPa)	1000 RPM			1400 RPM			1800 RPM		
	Min	Ave	Max	Min	Ave	Max	Min	Ave	Max
45 (mm/min)	180.6	193.1	205.7	187.1	197.6	208.2	158.2	164.3	170.5
60 (mm/min)	219.7	220.6	221.6	224.1	224.4	224.7	166.6	181.5	196.4
75 (mm/min)	205.9	209.4	212.9	173.0	175.3	177.6	200.2	202.5	204.9

Table 5 The optimum regression constants obtained for model in Eq. (1)

a	*b*	*c*	*d*	*e*	*f*	*g*
213.78834	−0.15400	−0.000095	−0.000016	−0.001180	0.00298	0.000043

the max UTS values (instead of the min values in Table 4) were fitted to, based on the best performance of the weld obtained under each process condition (i.e., a maxi–max design strategy). The highest coefficient of determination (R^2) of 0.955 was achieved when the following regression model was fitted to the max UTS values:

$$\mathrm{UTS}_{\mathrm{adj}} = a + bX_1 + cX_2 + dX_3 + bX_1^2 + cX_2^2 + dX_3^2 + eX_1X_2 + fX_1X_3 + gX_2X_3 \quad (1)$$

X_1 is the weld speed in mm/min, X_2 is the tool RPM, and X_3 is the average axial force in (N) from Table 3. The values of obtained model constants are given in Table 5.

Next, using the above regression model, the value of UTS at each given combination of RPM and weld speed was re-calculated/predicted, considering the corresponding constant average axial force. Results of the predictions are shown in Table 6, where the recalculated UTS values are called "adjusted" UTS hereafter. It is interesting that both samples 5n and 4n now demonstrate literally the same highest UTS values (marked in green). This is again in accordance with the hypothesis proposed in [20] about the cold weld condition and its positive effects on mechanical properties of FSW.

Next, the effect of each process parameters was evaluated using the UTS prediction function and constructing the main effect plots. Results of this analysis are shown in Fig. 14. For example in order to plot Fig. 14a, the values of total average weld speed and total average axial force were plugged into Eq. (1) as well as the individual values of three levels of the tool RPM. Figure 14 shows that the low weld speed, the high tool RPM (hot weld conditions), and the low axial force (low mechanical bonding) will minimize the UTS of FSW samples. This is again in accordance with the critical effect of hot weld condition on mechanical properties of FSW samples, by increasing the peak temperature and the heat-affected zone (HAZ) distance to the weld line. Figure 14 also shows that the high weld speeds and low tool RPMs (i.e., very cold weld conditions) can reduce the UTS of the FSW samples. The reason of low UTS in FSW samples with a cold condition would be the high viscosity and low mechanical bonding between material layers which rotate with tool and are deposited on the trailing edge. Generally speaking, the trends of main process factors in Fig. 14a, b, c show that there are non-moronic optimum values to be set for a FSW process in order to achieve the highest UTS in welded samples. If this optimum process window is exceeded, it can reduce the weld mechanical properties. In the experimental space under study, the global maximum UTS is reached when RPM=1,400, weld speed=60 mm/min (1 mm/s), and axial force=7.14 kN, which is the closest condition to that of sample 5n.

Finally, the percentage contribution of each process parameter was calculated following the relations in [20], along with their interaction effects, based on the adjusted UTS values considering the average value of the process parameters with the same total average of axial force for all the FSW samples. Results are shown in Fig. 15, suggesting that the highest effect in maximizing the UTS is related to the weld speed, followed by RPM. The interaction (error) is found to be as low as 2.5 %.

3.4 Examination of fracture surfaces

The fracture surfaces of all the FSW samples were examined as shown in Fig. 16. It was noticed that the samples with low UTS values have an S-shape fracture surface (samples 3n and

Table 6 Predicted max UTS values using the regression model

Adjusted Max UTS (MPa)	1000 RPM	1400 RPM	1800 RPM
45 (mm/min)	181.5	189.1	166.0
60 (mm/min)	226.4	226.9	196.8
75 (mm/min)	202.1	195.4	170.2

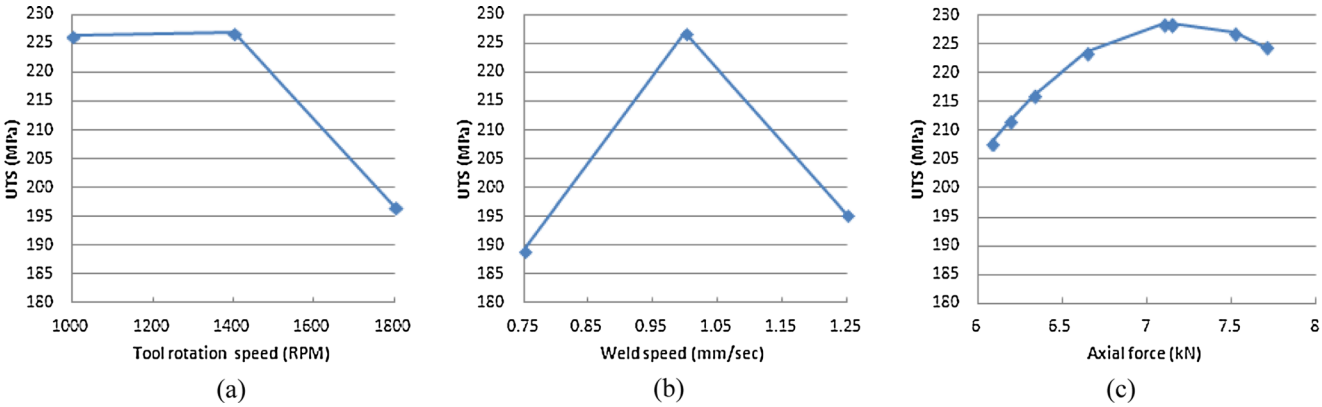

Fig. 14 Main effect plots based on the fitted regression model and average value of process parameters: **a** RPM, **b** weld speed, and **c** axial force

8n), and the samples with high UTS values have a ductile fracture surface with a necking region (samples 4n and 5n). It was also interesting that the set of samples from the same weld fractured at the same location with a similar fracture surface, indicating nearly uniform weld properties along the weld line.

Studying the fracture surfaces of tensile samples after tensile tests in more details, it was noticed that the material in the weld zone under the tool pin delaminated in sample 7n (cold weld) (Fig. 17) as a result of very low temperature (see Table 2), high viscosity, and low mechanical bonding of the welding material, which flows around the tool and merges again in the retailing edge of the tool during one rotation of the tool. A similar delamination also occurred in sample 2n (see Fig. 18) which had the lowest average axial force during FSW (Table 3) and a relatively high maximum temperature (Table 2). The delamination was similarly apparent in sample 3n which had the highest temperature during the welding and a relatively low axial force (Tables 2 and 3), probably because of the formation of thicker layers of aluminum oxide which can prevent mechanical bonding of the material during FSW in addition to the lack of sufficient contact force effect from a relatively low axial force of the tool (Fig. 19).

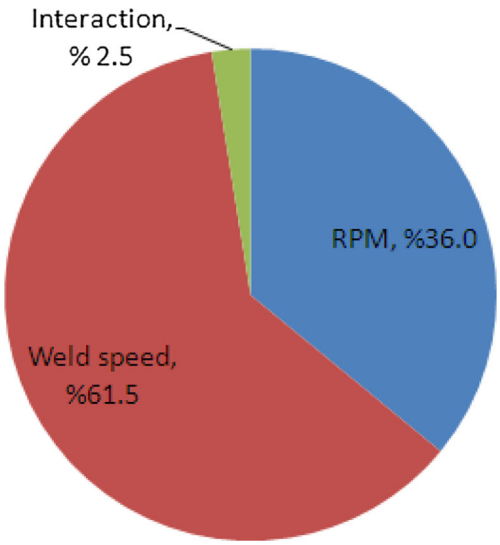

Fig. 15 Percentage contributions of the FSW process parameters on the weld UTS (the axial force has been considered to be fixed at its total average ~6.95 N)

Next, we performed microstructural analysis on the sample 5n with the highest UTS (highest average axial force) and sample 3n with the lowest UTS (hot weld) using a SEM. In sample 5n, different points of the fracture surface were studied as marked in Fig. 20. All over the sample, tiny cups and cones were noticed, which are representatives of ductile fracture with microvoid formation and coalescent as illustrated in Fig. 21.

In sample 3n, as seen before in the macro-level visual inspection of the tensile samples after fracture, the delamination of material under the tool pin has occurred (see both Figs. 19 and 22). When this delamination was examined by SEM, it was noticed (Fig. 23) that it also happens in other regions near the tool pin after tensile test fracture, with a uniform distance of the laminated layers equal to the advance-per-rotation of FSW; which is 25 μm/rotation (45/1,800=0.025 mm). Figure 23 is at the intersection of the continuation of an opened delaminate and the fracture surface on sample 3n after tensile testing fracture as marked by a yellow circle in Fig. 22. The yellow parallel lines in Fig. 23 were drawn with an equal distance of 0.025 mm which coincided with the tiny delaminated layers. In some regions of sample 3n, a low ductility fracture is observed with very small cups and cones compared to sample 5n as shown in Fig. 24. Also, in some regions of sample 3n (hot weld), the brittle fracture surfaces are noticed with cleavage as shown in Fig. 25. In brittle fracture regions, there were some areas of the inter-granular crack propagation with a sudden fracture evidence (see grains in Figs. 26 and 27).

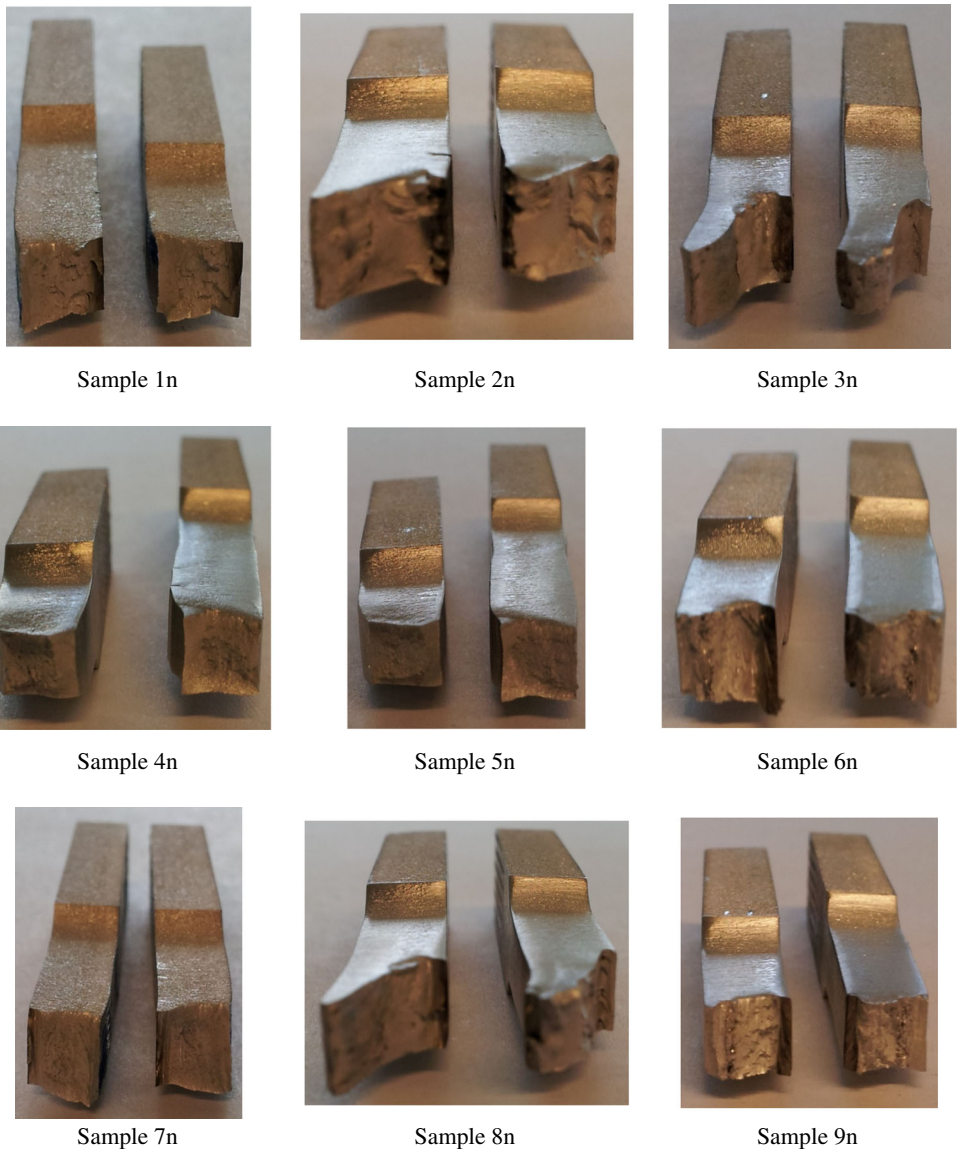

Fig. 16 Visual inspection of fracture surfaces of the samples with maximum UTS values

3.5 Electron back scattered diffraction (EBSD)

In this section, the grain size distribution at mid thickness of the advancing side of the weld zone was studied in sample 3n with lowest UTS (hot weld) and sample 5n with highest UTS and axial force. Results are shown in Fig. 28. For further analysis, in Fig. 28a, let us show the *x*-coordinates of some important regions of interest. Points A and B are at the tool's pin location (nugget zone), points C and D are at the tool's shoulder location, points E and F are at the middle points between the pin and the shoulder, points G and H are where the directional grains do not exist anymore (TMAZ ends and HAZ start), and points I and J are where the directional grains start to form (TMAZ start) in samples 3n and 5n, respectively.

From Fig. 28b, it can be seen that there is a relatively uniform dynamic recrystallized (DRX) grain size distribution in the nugget zone in both samples, and this average is higher in sample 3n with the highest maximum temperature during FSW. In the right hand side of points A and B where the tool's pin has not physically passed through the plate during FSW (but has been very close to it), there is a very low grain size region compared to the nugget zone in the left hand side of these points. Previously, a similar behavior was predicted in the microstructure modeling of aluminum 6061 using an integrated multiphysics numerical tool [21].

In Fig. 28c, one can clearly see the very low grain size in A–I and B–J regions which are near the tool pin from left hand side, followed by I–G and J–H regions with directional grains (TMAZ) in the right hand side. The A–I and B–J regions are shear zones (or rotation zones) with the same size of 1.35 mm in both samples 3n and 5n, which have had different maximum temperatures of 519 and 484 °C, respectively (see Table 2). This narrow region is where the material has a high rotation speed around the tool and can be defined during FSW

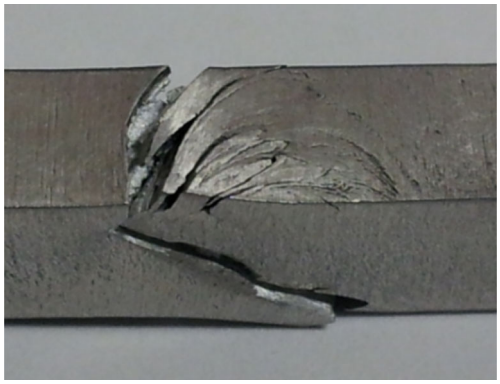

Fig. 17 Fracture zone under the tool pin in sample 7n (cold weld); notice the delaminated regions in vicinity of the weld line

multiphysics modeling using a stick coefficient (δ) and the tool rotational speed [22]. If the material is trapped in the shear layer, its deposit is delayed and may rotate with the pin more than one cycle, which causes a higher strain rate and more grain refinement during DRX. It is important to notice that the shear layers have had the same thickness in both hot and relatively cold samples. It is also interesting that the length of TMAZ region in sample 3n (hot weld) with maximum temperature of 519 °C is higher than sample 5n with maximum temperature of 484 °C. Also, the directional grain in TMAZ of sample 3n are more toward the horizontal line compared to sample 5n.

In Fig. 28d, one can notice that the HAZ starts after the end of directional grains in the TMAZ. The size of grains in HAZ regions near TMAZ are increased compared to the base metal grains, which are at the right hand side of the figure. The grain growth in the HAZ of sample 3n (hot weld) is higher compared to sample 5n (relatively cold).

3.6 Microhardness and number of grains

In this section, the microhardness (HV) distribution and also the number of grains on a length of 77 μm (horizontal line)

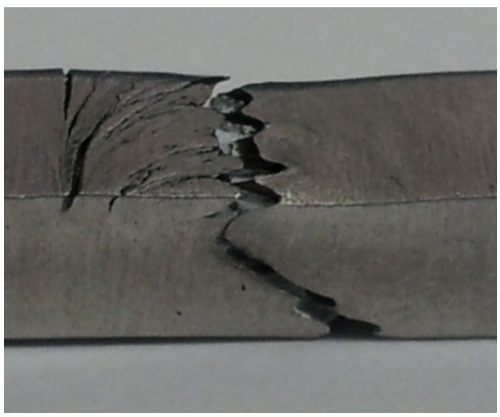

Fig. 18 Fracture zone under the tool pin using sample 2n with the lowest average axial force; notice the delaminated regions in vicinity of the weld line

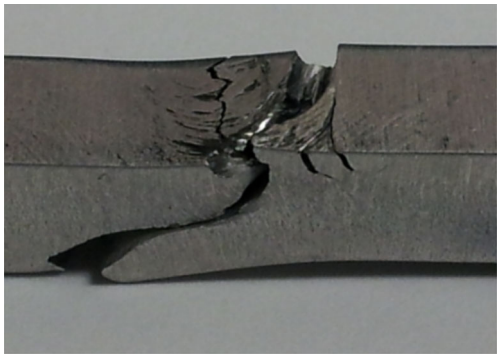

Fig. 19 Fracture zone under the tool pin in sample 3n (hot weld); notice the delaminated regions in vicinity of the weld line

were measured at different points of samples 3n and 5n. Results are shown in Fig. 29.

From Fig. 29, in the nugget zone (left hand side of points A and B), once can see that the number of grains is higher in sample 5n compared to sample 3n (hot weld). In other words, sample 5n (relatively cold weld) has had a lower average grain size in the nugget zone compared to sample 3n (hot weld), which would have been resulted from the lower temperature during dynamic recrystallization and grain growth in sample 5n. Relatively higher values of hardness are also noticed in sample 5n compared to sample 3n in the nugget zone.

In the regions A–I and B–J in Fig. 29, there is an evidence of shear layers (rotation layer) in samples 3n and 5n, respectively. More specifically, in these regions again, the grain size of the sample 5n is lower compared to the sample 3n which also causes a higher hardness in sample 5n. Also, in both

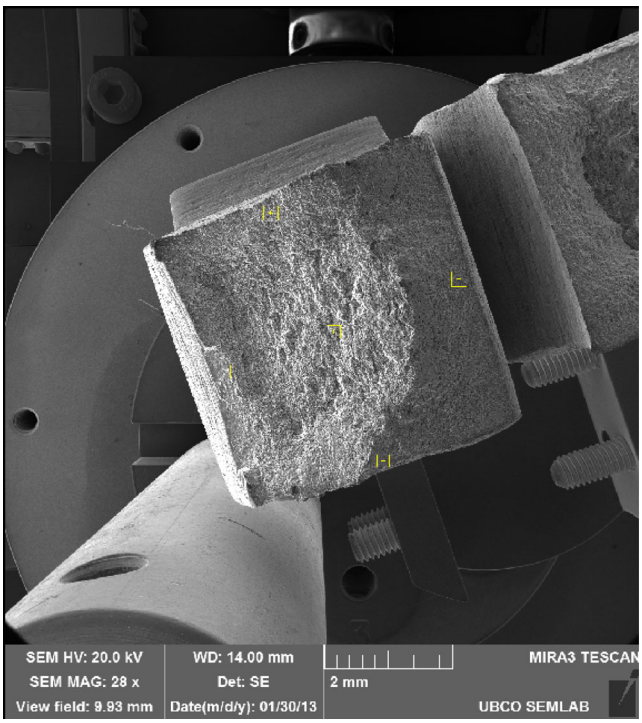

Fig. 20 Fracture surface of sample 5n with the highest UTS (×28)

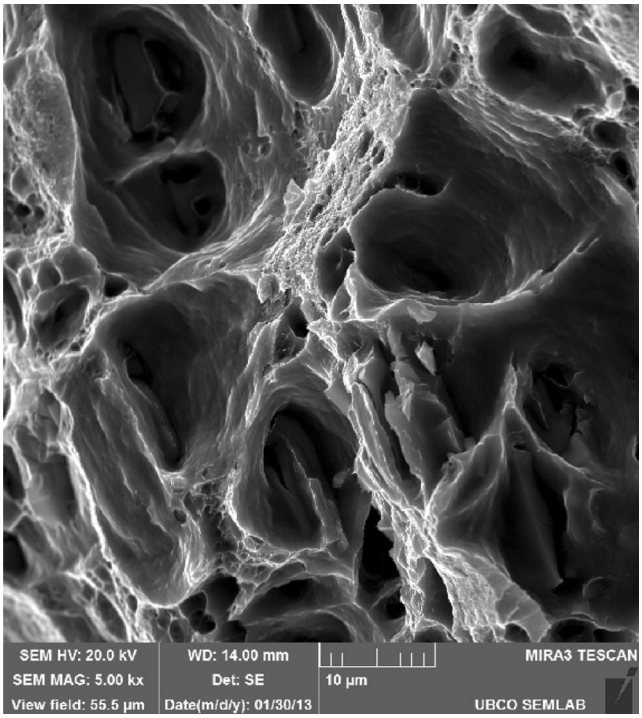

Fig. 21 Typical high magnification of fracture surface in sample 5n with the highest UTS (×5,000)

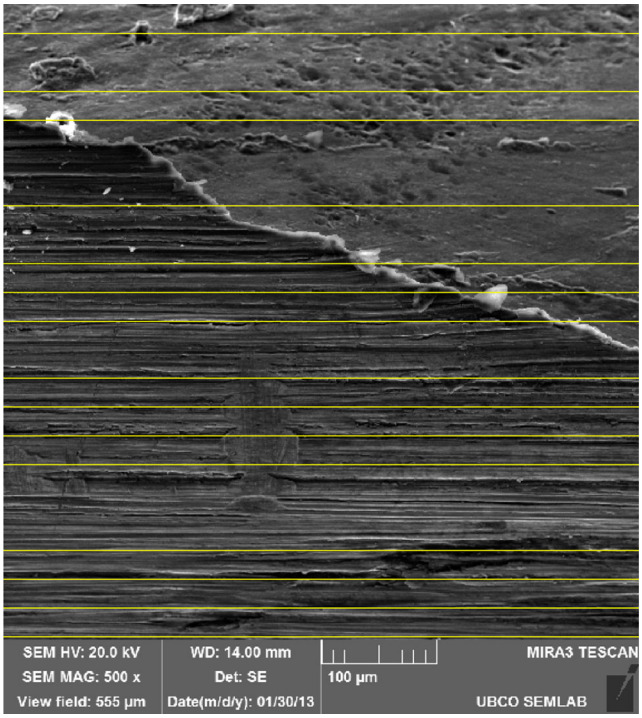

Fig. 23 Distances between laminates at *yellow circle* in Fig. 22 using higher magnification (×500)

samples in the middle of shear layer, the number of grains decreases or the average grain size increases, causing a decrease in the corresponding microhardness.

In regions I–G and J–H, one can see the thermomechanically affected zone (TMAZ) of samples 3n and 5n, respectively, with the directional grains with larger sizes compared to the base metal, indicating the occurrence

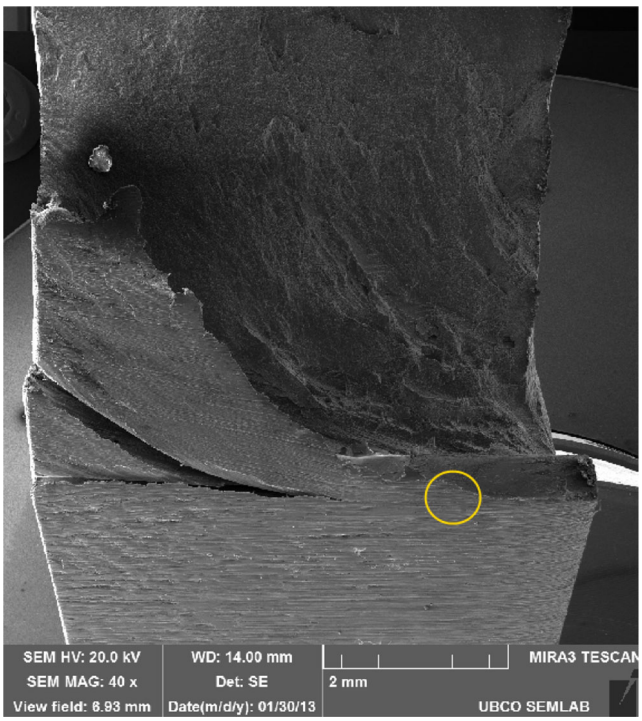

Fig. 22 Delamination in the material under the tool pin in sample 3n or hot weld (×40)

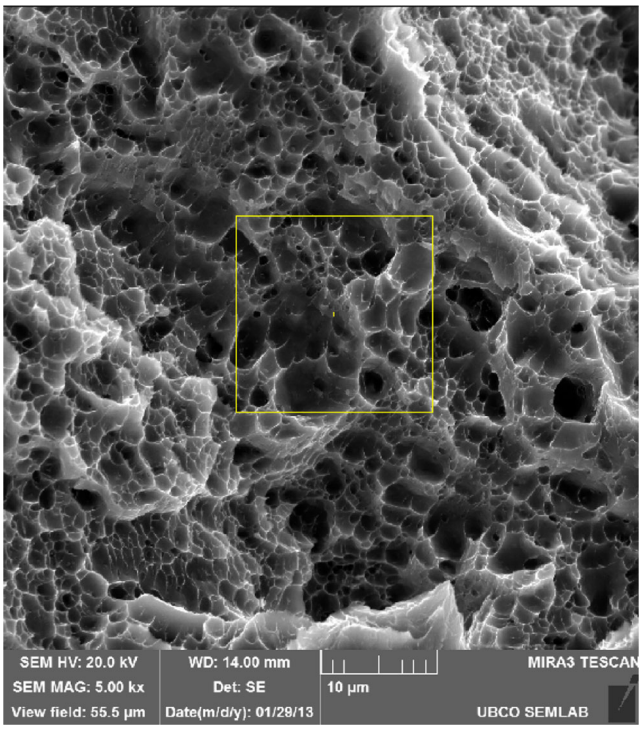

Fig. 24 Low ductility fracture in some regions of sample 3n or hot weld (×5,000)

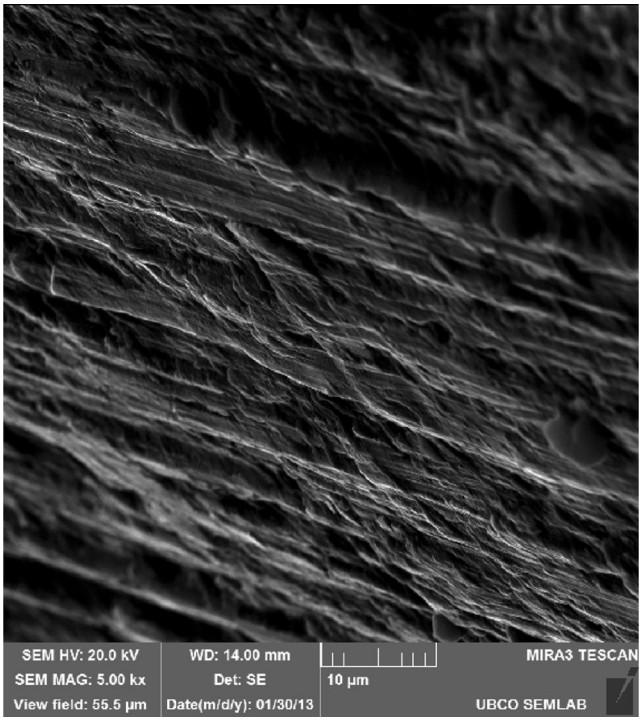

Fig. 25 Brittle fracture in some regions of sample 3n or hot weld (×5,000)

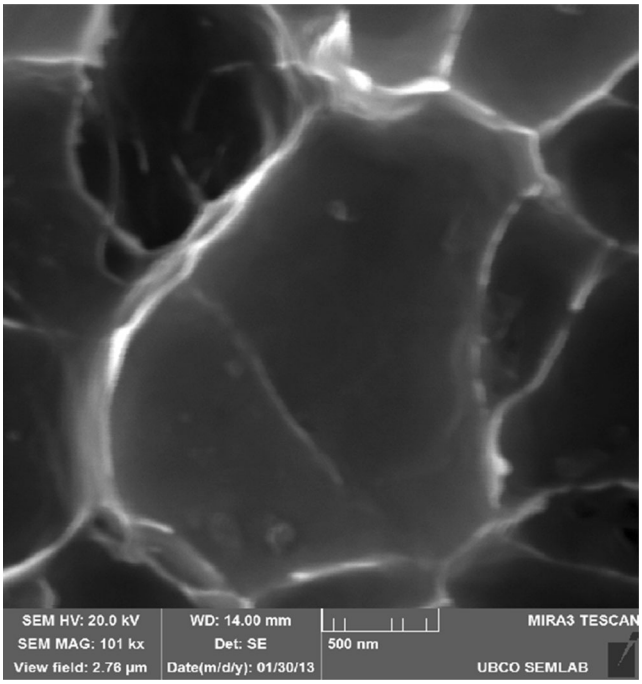

Fig. 27 Inter-granular fracture in sample 3n with very high magnification (×101,000)

of grain growth in TMAZ during FSW. In the TMAZ region of sample 3n, near its shear zone, still some dynamic recrystallization happens, which causes a lower grain size as compared to sample 5n in the same region. Looking at the right hand side of the TMAZ, it can be noticed that the directional grain size in sample 5n (highest UTS and relatively cold weld) becomes smaller compared to sample 3n (hot weld). The total length of the TMAZ of sample 3n (I–G) is higher than the one in sample 5n (J–H) (I–G=~3.75 mm and J–H=~3.12 mm).

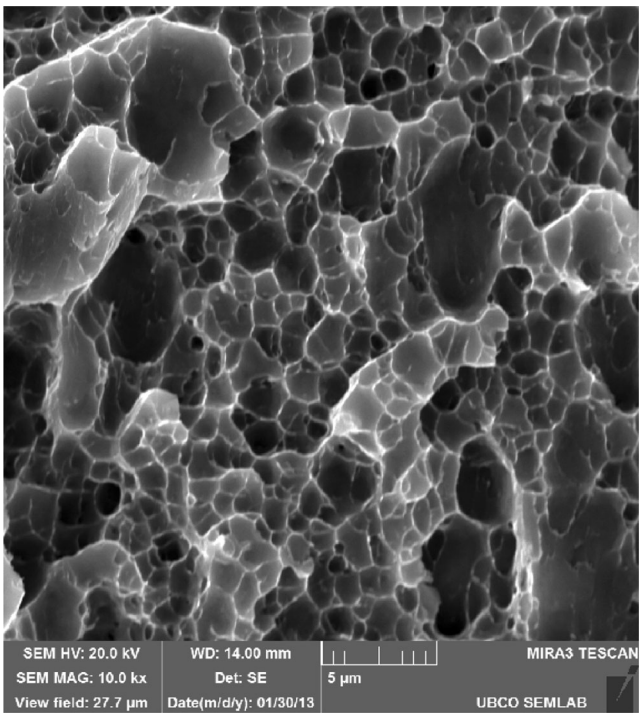

Fig. 26 Inter-granular fracture in sample 3n (hot weld) with the lowest UTS (×10,000)

The minimum hardness in both samples happens at the interface of TMAZ and HAZ where both samples have similar grain size values. This shows the effect of precipitates size, coherency to matrix, and their distribution on the formation of the minimum hardness location. It was also previously predicted via a numerical study [20] that the minimum hardness location is located at the interface of TMAZ and HAZ. The minimum hardness of sample 5n (relatively cold weld) is higher than the one in sample 3n (hot weld) where it occurs at a closer location to the weld line compared to sample 3n. The latter observation complies with the idea proposed in [20]: The lower the peak temperature and the HAZ distance to the weld line, the lower the hardness decrease of the FSW samples. In addition, it was addressed in Section 3.4 that if the FSW weld is very cold, the low mechanical bounding deteriorates the mechanical properties of FSW samples. From Fig. 29, in both regions of HAZ which are very close to TMAZ, we can see the grain growth in both samples 3n and 5n, while the extent of this growth is higher in sample 3n (hot weld) due to the higher maximum temperature during FSW.

Finally, when the right hand side of the HAZ in both samples 3n and 5n is inspected in Fig. 29, no grain growth is

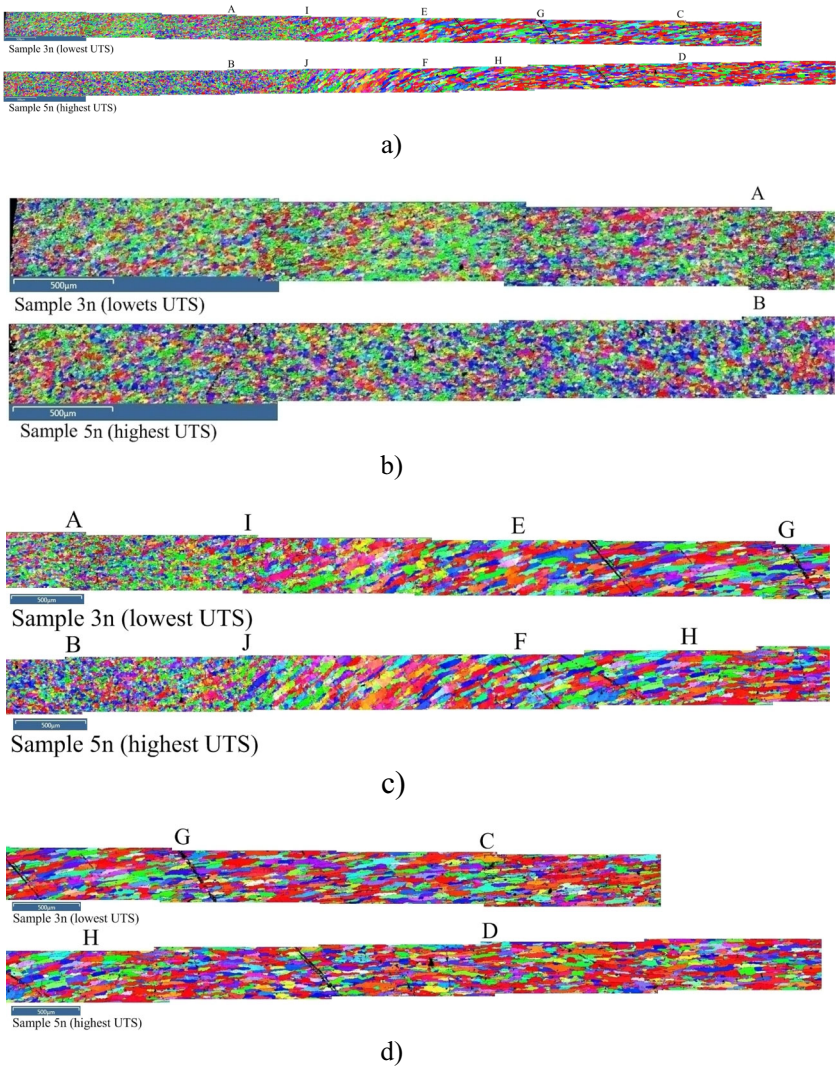

Fig. 28 Grain size distribution at mid thickness of the advancing side of the weld zones of sample 3n with the lowest UTS (hot weld) and sample 5n with the highest UTS; **a** the whole profile; **b** higher magnification of the nugget zone and shear layer; **c** higher magnification of shear layer and thermomechanically affected zone (TMAZ); **d** higher magnification of the TMAZ, heat-affected zone (HAZ), and base metal

noticed and their grain sizes have been equal to that of the base metal. The steep hardness increase from the HAZ toward the base metal region is the result of the FSW heat and its effect on the precipitates size, coherency to matrix and distribution as explained in [20]. The base metal hardness is recovered in higher distances to the weld line in sample 3n (hot weld) compared to sample 5n (relatively cold weld) as a result of higher maximum temperature in sample 3n during welding.

4 Summary of main conclusions

Based on the above experimental and optimization study on aluminum 6061, the following main conclusions may be made on relationship of process parameters, microstructure, and mechanical properties of the FSW welds:

- The maximum temperature is reduced by increasing the weld speed under a constant tool RPM during FSW.
- The maximum temperature is increased by increasing the tool RPM under a constant weld speed during FSW.
- The highest axial force during steady-state phase of FSW occurs in sample 7n (cold weld), and the lowest axial force occurs in sample 3n (hot weld).
- The highest torque is seen in sample 7n (cold weld) and also occasionally in sample 4n (second cold weld). The lowest torque happens in sample 3n (hot weld).
- When the RPM is increased with a constant weld speed, the torque is decreased during FSW.
- The highest UTS in the FSW samples had a UTS equal to 0.76 of the as-received plate.
- The minimum transverse force is seen in sample 4n, and the maximum transverse force belongs to samples 6n and 9n with the highest RPM and sometimes to sample 7n (cold weld). The highest transverse force in samples 6n and 9n or 7n may have been resulted from higher excess

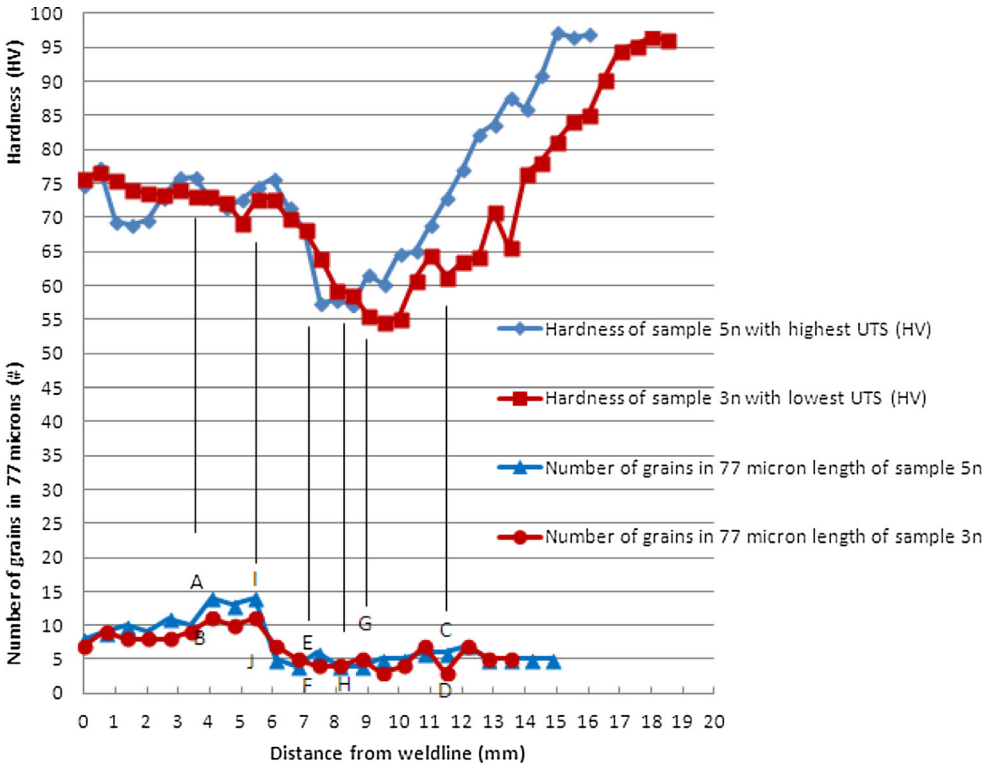

Fig. 29 Microhardness (HV) and the number of grains in a 77 μm horizontal line at different locations of samples 3n and 5n with the lowest and the highest UTS values, respectively

material from the weld (flush) or a higher material flow stress during FSW, respectively.

- The time distance between two consecutive transverse force peaks is equal to the time of advance per rotation during FSW.
- The samples 3n, 6n, and 9n with the highest tool RPM values and sample 5n with the highest average axial force had a high volume of excess material from the weld zone (flush).
- In samples 1n, 6n, and 9n which had the lack of diffusion failure, a relatively higher transverse force during FSW was seen, which would be due to the higher excess material from the weld zone (flush).
- The minimum UTS belonged to sample 3n (hot weld), and the maximum UTS is seen in both samples 5n (highest average axial force) and 4n (second cold weld) with small difference in UTS.
- Based on the regression model at the same average axial force, both samples 5n (highest average axial force) and 4n (second cold weld) showed literally the same highest UTS values.
- There are optimum values to set the FSW process parameters in order to get the highest UTS in the weld. If one exceeds the optimum processing window, it can reduce the weld mechanical properties.
- All the samples with low UTS values had an S-shape fracture surface (samples 3n and 8n), and the samples with high UTS values had a ductile fracture surface with necking region (samples 4n and 5n).
- When the temperature is very low or very high or axial force is very low during FSW, the material under the tool's pin in the weld zone after tensile test fracture showed the delamination which is a result of low mechanical bounding between layers of material rotating around the pin and forming the weld.
- Based on the SEM studies on fracture surfaces after tensile tests, sample 5n with the highest UTS and axial force values had a ductile fracture surface and sample 3n (hot weld) with the lowest UTS had both low ductility and brittle fracture surfaces.
- There is a relatively uniform DRX grain size in the nugget zone in both samples 3n (hot weld) and 5n (relatively cold weld), and on average, it is higher in sample 3n having a higher maximum temperature during FSW.
- Shear layer had the same thickness in both sample 3n (hot weld) and 5n (highest UTS and axial force) equal to 1.35 mm. Note that grain size in sample 3n (hot weld) was smaller compared to sample 5n (relatively cold weld). In the middle of both shear layers, there are slightly larger grains.
- The length of TMAZ region in sample 3n (hot weld) is higher compared to sample 5n (relatively cold weld). Also, the directional grains in the TMAZ of sample 3n are more toward the horizon line compared to sample 5n.
- The sizes of grains in HAZ near TMAZ are increased in both samples 3n and 5n, while the increase is more significant in sample 3n (hot weld).

- In the TMAZ of sample 3n near its shear zone, still some dynamic recrystallization happens and causes a lower average grain size compared to sample 5n in the same position. Looking at the right hand side of the TMAZ, we noted that the directional grain size in sample 5n (relatively cold weld) becomes smaller compared to sample 3n (hot weld).
- The total length of TMAZ of sample 3n (hot weld) is higher than the one in sample 5n (relatively cold weld).
- The minimum hardness in both samples 3n and 5n happens at the interface of TMAZ and HAZ. The precipitates size and their distribution cause the hardness decrease.
- The minimum hardness of sample 5n (relatively cold weld) is higher than that of sample 3n (hot weld), and it happens at a closer location to the weld line.
- In border regions of HAZ close to TMAZ, the grain growth happens in both samples 3n and 5n where the amount of grain growth is higher in sample 3n (hot weld) due to the higher maximum temperature during FSW.
- The base metal hardness is recovered at higher distances to the weld line in sample 3n (hot weld) compared to sample 5n (relatively cold weld) due to higher maximum temperature in sample 3n (hot weld).

Acknowledgments The authors wish to acknowledge financial support from the Natural Sciences and Engineering Research Council (NSERC) of Canada. Also, the guidance and assistance of Dr. A. Phillion from the University of British Columbia during EBSD tests are greatly recognized.

References

1. Yan J, Sutton M, Reynolds A (2005) Process-structure-property relationships for nugget and heat affected zone regions of AA2524-T351 friction stir welds. Sci Technol Weld Join 10:725–736
2. Mahoney M, Harrigan W, Wert J (1998) Friction stir welding sic discontinuously reinforced aluminum, INALCO, Seventh Int. Conf. Joints in Aluminum (Cambridge, U.K.)
3. Commin L, Dumont M, Masse J-E, Barrallier L (2009) Friction stir welding of AZ31 magnesium alloy rolled sheets: influence of processing parameters. Acta Mater 57:326–334
4. Lee W-B, Jung S-B (2004) The joint properties of copper by friction stir welding. Mater Lett 58:1041–1046
5. Konkol PJ, Mathers JA, Johnson R, Pickens JR (2003) Friction stir welding of HSLA-65 steel for shipbuilding. J Ship Prod 19:159–164
6. Posada M, DeLoach J, Reynolds AP, Skinner M, Halpin J (2001) Friction stir weld evaluation of steel and stainless steel weldments. Proceedings of the Symposium on Friction Stir Welding and Processing, TMS 2001, 159–171
7. Nandan R, Lienert TJ, DebRoy T (2008) Toward reliable calculations of heat and plastic flow during friction stir welding of Ti-6Al-4V alloy. Int J Mater Res 99:434–444
8. Aval HJ, Serajzadeh S, Kokabi AH (2011) Thermo-mechanical and microstructural issues in dissimilar friction stir welding of AA5086–AA6061. J Mater Sci 46:3258–3268
9. Taban E, Gould JE, Lippold JC (2010) Dissimilar friction welding of 6061-T6 aluminum and AISI 1018 steel: properties and microstructural characterization. Mater Design 31:2305–2311
10. da Silva AAM, Aldanondo E, Alvarez P, Echeverría A (2010) Dissimilar joining of AA1050 aluminium alloy and hot-stamped boron steels using friction stir, friction stir spot welding and friction stir shoulder welding. 8th international FSW symposium TWITimmendorfer Strand, Germany
11. McLean AA, Powell GLF, Brown IH, Linton VM (2003) Friction stir welding of magnesium alloy AZ31B to aluminium alloy 5083. Sci TechWeld Join 8:462–464
12. Somasekharan AC, Murr LE (2004) Microstructures in friction-stir welded dissimilar magnesium alloys and magnesium alloys to 6061-T6 aluminum alloy. Mater Charac 52:49–64
13. Uzun H, Dalle Donne C, Argagnotto A, Ghidini T, Gambaro C (2005) Friction stir welding of dissimilar Al 6013-T4 To X5CrNi18-10 stainless steel. Mater Design 26:41–46
14. Ouyang J, Yarrapareddy E, Kovacevic R (2006) Microstructural evolution in the friction stir welded 6061 aluminum alloy (T6-temper condition) to copper. J Mater Proc Tech 172:110–122
15. Dressler U, Biallas G, Mercado UA (2009) Friction stir welding of titanium alloy TiAl6V4 to aluminium alloy AA2024-T3. Mater Sci Eng A 526:113–117
16. Chung YD, Fujii H, Tanigawa H (2010) Dissimilar friction stir welding of F82H steel and austenite stainless steels without transformation. 8th international FSW symposium TWI Timmendorfer Strand, Germany
17. Mishra RS, Mahoney MW (eds) Friction stir welding and processing. ASM International®. Materials Park, Ohio
18. Woo W, Choo H (2006) Texture analysis of a friction stir processed 6061-T6 aluminum alloy using neutron diffraction. Acta Mater 54: 3871–3882
19. Frankel G, Xia Z (1999) Localized corrosion and stress corrosion cracking resistance of friction stir welded aluminum alloy 5454. Corrosion 55:139–150
20. Nourani M, Milani AS, Yannacopoulos S (2011) Taguchi optimization of process parameters in friction stir welding of 6061 aluminum alloy: a review and case study. Eng 3:144–155
21. Nourani M, Milani AS, Yannacopoulos S, Yan C (2012) Predicting grain size distribution in friction stir welded 6061 aluminum alloy. Proceedings of 9th International Friction Stir Welding Symposium, TWI, Huntsville
22. Nourani M, Milani AS, Yannacopoulos S, Yan C (2014) An integrated multiphysics model for friction stir welding of 6061 aluminum alloy. Int J Multiphys 8(1):29–48